ORIGINAL RESEARCH ARTICLE

Development of a Dross Build-Up Growth Process Model for Hot-Dip Galvanizing Considering Surface Reaction Kinetics

GEORG REISS, WERNER EßL, RALUCA ANDREEA TRASCA, CLAUDIA MUGRAUER, MIHAELA STEFAN-KHARICHA, ABDELLAH KHARICHA, EVA GEROLD, and FRANK GOODWIN

The minimization of unwanted dross build-up formation on the sink rolls in continuous hot-dip galvanizing lines is a key goal of the industry. In this study, the CFD multi-physics modeling of the surface reaction kinetics for dross build-up growth and the coupling to the mass transfer is the basis for the evaluation of relevant process parameters. The results of a virtual Design of Experiments were processed by neural network approaches, as well as linear regression modeling to build a surrogate process model. It was found that the bath Al concentration has the highest effect (> 80 pct) on the dross build-up rate on the sink rolls. Operating the zinc bath at higher Al concentrations decreases the dross build-up reaction rate. Furthermore, it was found by the CFD multi-physics model that the local dross build-up rate increases toward the edges of the roll grooves which might lead to the occurrence of strip surface defects.

https://doi.org/10.1007/s11663-023-02921-2

I. INTRODUCTION

CONTINUOUS hot-dip galvanizing of steel strips is the main process for zinc corrosion protection of autobody parts. The inclusion of small amounts of Al (0.1–0.3 wt pct) in the liquid Zn increases the adherence of the Zn layer by the formation of an Fe_2Al_5-inhibition layer. However, the concurrent dissolution of Fe from the steel strip in the liquid zinc bath leads to a ternary Zn–Al–Fe system that can cause the formation of floating Fe_2Al_5 particles in the liquid Zn or solid dross build-up on the bath equipment.[1] Especially the dross build-up on the rolls can deteriorate the surface quality of the steel strip significantly and leads to frequent maintenance cycles. Figure 1 shows the dross build-up on the sink roll after the production cycle. New demands for thinner coatings without drawbacks in corrosion resistance lead to increasing challenges in the process, to avoid dross build-up-induced surface defects.

The main question is how to reduce the dross build-up? One approach is to improve the coating and sealing of the sink rolls to reduce the nucleation rate and thus the growth on the sink rolls. State-of-the-art coating of the sink rolls is a WC-Co coating[2] which improves wear resistance for the contact of the steel strip and the roll. It is, however, known that the liquid Zn attacks this coating and forms Zn–Co phases that lead to a disintegration of the coating.[3,4] Thus, also sealers (*e.g.,* Boron–Nitride:Potassium–Silicate) are applied to protect the coating from the liquid Zn–Al solution.[1] In addition to that, coatings based on other materials (*e.g.,* Al_2O_3)[2] are developed and the application of different layers is patented (*e.g.,* Ni–Co–Cr base layer, Mo-Cerment, ceramic containing stabilized ZrO_2).[5,6] However, experiments have shown that dross build-up occurs on the coatings and that hydrodynamics plays an important role, which means that nucleation and growth cannot be avoided entirely.[1] This can be explained by the thermodynamic concept of the nucleation tendency of dross particles developed in Reference 7, where a homogeneous nucleation in the liquid melt was computed. In general, a heterogeneous nucleation on the sink roll surface requires a lower driving force compared to homogeneous nucleation. Another approach to minimize dross build-up is to control the bath management (*e.g.*, temperature ramps, concentration changes) to

GEORG REISS, WERNER EßI, RALUCA ANDREEA TRASCA, and CLAUDIA MUGRAUER are with the Materials Center Leoben Forschung GmbH, Roseggerstraße, 12, Leoben 8700, Austria. Contact e-mail: georg.reiss@mcl.at MIHAELA STEFAN-KHARICHA, ABDELLAH KHARICHA, and EVA GEROLD are with the Montanuniversität Leoben, Franz-Josef-Straße 18, Leoben 8700, Austria. FRANK GOODWIN is with the International Zinc Association, 1000 Park Forty Plaza, Durham, NC 27713.

Manuscript submitted May 11, 2023; accepted September 8, 2023.
Article published online November 10, 2023.

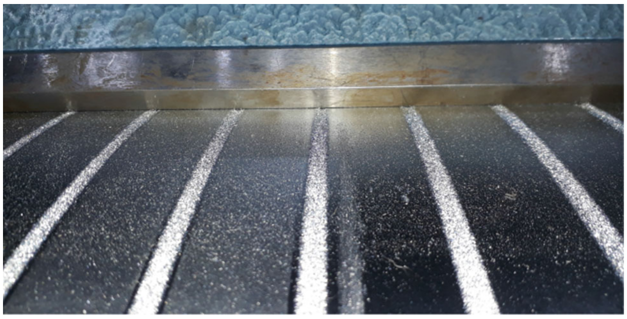

Fig. 1—Dross build-up (Fe_2Al_5) on the sink roll (by courtesy of Michel Dubois).

ensure that the growth rate of the dross build-up is as low as possible. In this context, the main source of Fe is the dissolution from the steel strip. It was shown that in the very beginning, when the steel strip first enters the liquid Zn, a meta-stable equilibrium prevails that leads to a significantly higher Fe dissolution.[8] This Fe causes a supersaturation in the zinc bath which is then reduced by the formation and growth of floating dross particles and the formation of dross build-up on the sink rolls. The understanding of the distribution of this supersaturation of Fe and the growth of the dross build-up layer is of the utmost importance to the line operator in order to control the process conditions to minimize the dross build-up growth.

While the process conditions, such as line-speed or strip temperature can be measured quite easily, the size of the zinc bath and the harsh environment limits capabilities for detailed measurements to a few locations, which are far away from the rotating roll surface. Therefore, CFD simulation methods were developed in the past decades to offer more insight into the temperature and species distributions in the zinc bath.[9–14] These works focused on the identification of the dross formation rates. The approaches included thermodynamics considerations and were significantly improved by a reversible reaction kinetics model.[15]

However, none of these models addressed the growth of the dross build-up on the roll surfaces. Stefan-Kharicha *et. al*.[16] developed a front-tracking crystal growth model that is capable of coupling the mass transfer toward the surface with the growth of the dross crystals. It was found that the growth rates for rotating equipment was higher than for stationary, which is in accordance to measurements.[1] Nevertheless, to resolve the diffusion boundary layer and accurately describe the mass flux, a very fine computational mesh was required which limited the simulation to a 2-D domain with a size of 300 μm. Other works on an atomic length scale focus on the determination of the surface energies and adhesion forces between the sink roll and the dross.[17]

In this paper, we present a set of methods to build a process model to predict dross build-up growth depending on the process parameters. A surface reaction model for dross build-up was coupled with the convective and diffusive mass transport via the wall function approach. A mesh independent formulation of the dimensionless wall concentration is presented that is used to model the growth of the dross build-up with a quadratic growth law. It is thus possible, to determine the influence of process parameters on the actual roll dross build-up growth and to establish a process model based on linear regression modeling and neural networks. Moreover, statistical evaluation tools using the software *R* have been applied to quantify the most important parameters that affect dross build-up growth.

II. METHODS

In this chapter, first the model set-up of the geometry, the mesh, the boundary conditions, and the material parameters are described. Then the theoretical background for modeling the surface concentrations and reactions is summarized. Next the conduction of the virtual Design of Experiments is presented and finally, the neural network and linear regression modeling approaches to develop the surrogate process model are described.

A. *Model Set-Up*

A section of the zinc bath, namely the V-shaped region between the incoming and outgoing steel strip, is modeled in this study with *AnsysFluent* v21.2. The geometry consists of a 3-D slice of this V-shaped region including the repetition of a sink roll groove. The width of this slice is $\sim$ 16 mm bounded by symmetry planes at front and back (see Figure 2).

The fluid flow of the liquid zinc is computed by solving the continuity:

$$\frac{\partial \rho}{\partial t} + \nabla \cdot (\rho \boldsymbol{u}) = \boldsymbol{0}, \qquad [1]$$

and Navier–Stokes equations with the finite volume method.[18] A classical approach to account for turbulence is the Reynolds averaging, where the instantaneous equations are decomposed into mean and fluctuating components.[19] Time-averaging of these equations yields the Reynolds-averaged Navier–Stokes (RANS) equations:

$$\frac{\partial \rho \boldsymbol{u}}{\partial t} + \boldsymbol{u} \cdot \nabla \rho \boldsymbol{u} = -\nabla p + \nabla \cdot \left(\mu \nabla \boldsymbol{u} - \boldsymbol{\tau}'_{ij} \right) - \rho \boldsymbol{g} \beta_{\mathrm{T}} (T - T_0) \qquad [2]$$

where $\boldsymbol{u}$ is the velocity (m s^{-1}), ρ is the density (kg m^{-3}), p is the pressure (Pa), μ is the dynamic viscosity (Pa s) and the last term accounts for the buoyancy caused by temperature T (K) variations. Local changes of the density are modeled with a thermal expansion coefficient β_{T} (K^{-1}) and the gravity vector $\boldsymbol{g}$ (m s^{-2}).[9]

The additional term $\boldsymbol{\tau}'_{ij}$ (Reynolds stresses) is a result of the Reynolds averaging and has to be modeled in order to close Eq. [2]. One approach is to apply the $k-\omega$ Shear-Stress Transport (SST) model that solves two additional equations for turbulent kinetic energy k and the specific dissipation rate ω. The $k-\omega$ approach is

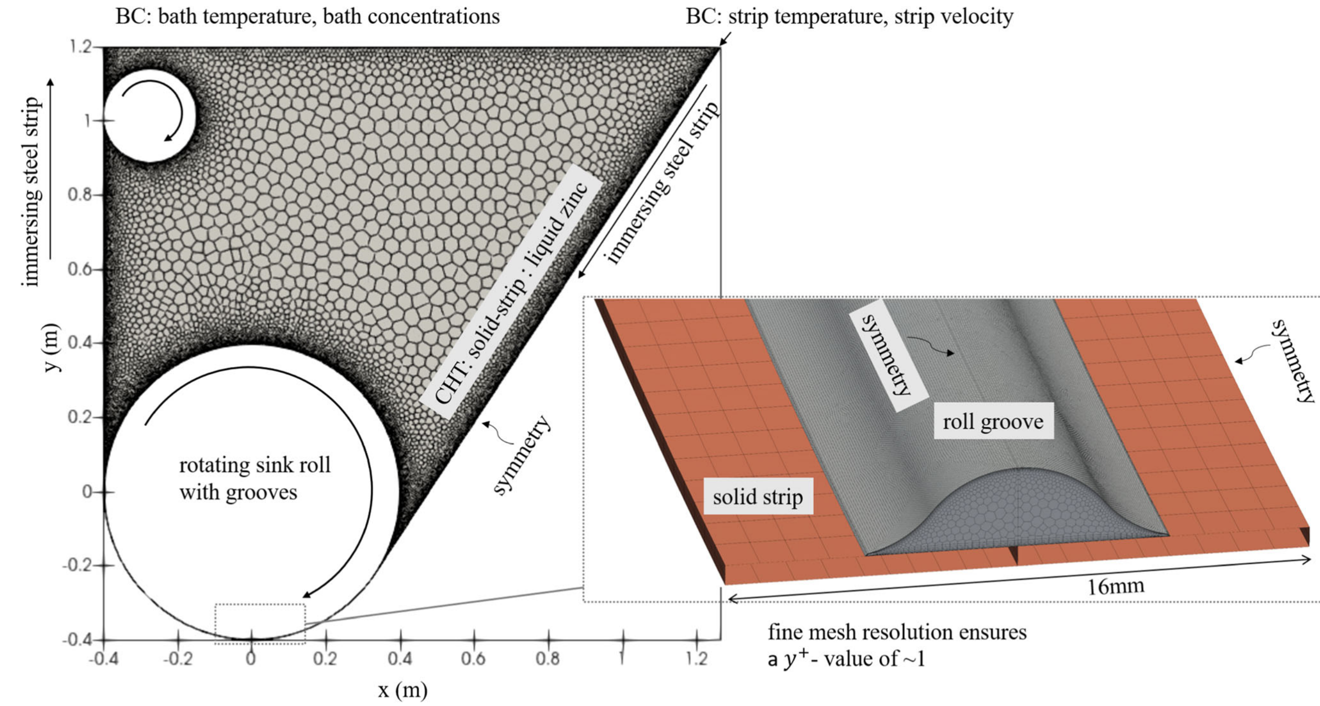

Fig. 2—Left: 3-D model geometry of a 16 mm slice of the V-shaped region of the zinc bath with symmetry boundary conditions in z-direction. Right: Detailed view of the mesh resolution in the sink roll grooves.

superior to the standard $k-\epsilon$ model especially close to walls and yields a better description of the turbulence.[20] A fine mesh resolution was chosen to achieve a y^+-value of 1 and a smooth transition to the rest of the domain resulting in 29mio. computational cells.

The energy equation in the liquid zinc is coupled with the solid steel strip via a Conjugated Heat-Transfer (CHT) approach. The steel strip is modeled as moving solid with a prescribed immersing velocity and entry temperature. It is assumed that the incoming steel-strip energy is distributed evenly to both strip sides. As only the V-region of the zinc bath and thus one strip side is modeled, only half of the incoming steel-strip energy is coupled with the simulation domain. The details on the solution of the species transport equations and the surface reactions are described in detail in Section II–B.

The boundary conditions for the temperature and Al concentration are set at the top of the domain (see Figure 2), representing averaged bath values, while for the Fe concentration, a slight supersaturation of 10 pct is assumed.

The material parameters for the liquid zinc and the solid steel strip are reported in Reference 14. The additional Fe dissolution and Al uptake at the steel-strip interface are modeled according to Reference 14. The reaction kinetics constant K = 4.5 m s^{-1} for the surface reaction model in Eq. [8] was determined by means of ab-initio based kinetic Monte–Carlo simulation in Reference 21. The developed surface concentration model for the build-up is described as follows in Chapter 2.2.

B. *Modeling of Surface Concentrations*

A detailed model description of the thermo-chemical turbulent flow modeling in zinc baths can be found in Reference 14 and the development of a first reversible reaction kinetics model is presented in Reference 15. In this model, in addition to the flow, turbulence, and energy, the species transport equations for the concentrations of Al and Fe are solved:

$$\frac{\partial \rho y_i}{\partial t} + \boldsymbol{u} \cdot \nabla \rho y_i = \nabla \cdot \left(\rho \left(D_{ij} + D_{\mathrm{t}} \right) \nabla y_i \right) + q_{\mathrm{R_i}} + q_{\mathrm{I_i}} + q_{\mathrm{S_i}}, \quad [3]$$

where y_i is the mass fraction of species i (*e.g.*, Al, Fe, Fe_2Al_5, $FeZn_7$ that are present in galvanizing baths), D_{ij} (m^2 s^{-1}) is the binary diffusion coefficient and D_t is the turbulent diffusivity. The terms $q_{\mathrm{R_i}}$, $q_{\mathrm{I_i}}$ and $q_{\mathrm{S_i}}$(kg m^{-3} s^{-1}) are species source terms due to chemical reactions, ingot melting and reactions at the strip surface. The modeling of these source terms is discussed in more detail in References 14 and 15.

The solution of Eq. [3] in the volume is straightforward given the correct set of boundary conditions. One major problem arises when surface reactions have to be taken into account. In this case, the very thin diffusion boundary layer has to be properly described to compute the mass transfer toward the surface accurately. This can be done firstly by creating a very fine mesh in the vicinity of the walls to be able to directly compute the diffusion boundary layer. However, this approach is not feasible in terms of computational time because a very high number of computational cells would be required. The second approach is the modeling of the diffusion boundary layer based on the law-of-the-wall theory. Depending on the mesh resolution at the wall interface, three different regions can be discerned, based on the dimensionless wall distance y^+[19]: First, a linear region at small y^+-values, where the diffusion boundary layer can be resolved, second a buffer layer, and third the logarithmic region, where the diffusion boundary layer is modeled via wall function. The graphical representation is shown in Figure 3.

The wall functions for species transport are defined in analogy to the temperature as described in Reference 22:

$$Y^* \equiv \frac{(y_{i,w} - y_i)\rho c_\mu^{1/4} k_p^{1/2}}{J_{i,w}}, \qquad [4]$$

where Y^* is the dimensionless concentration, $y_{i,w}$ and y_i are the wall and wall-adjacent cell center mass fractions, ρ is the density, c_μ is a turbulence constant, k_p is the turbulent kinetic energy at the wall-adjacent cell center, and $J_{i,w}$ is the diffusion flux of species i at the wall.

To be independent of the mesh resolution, Y^* can be defined with a blending of the sublayer and logarithmic region[23]:

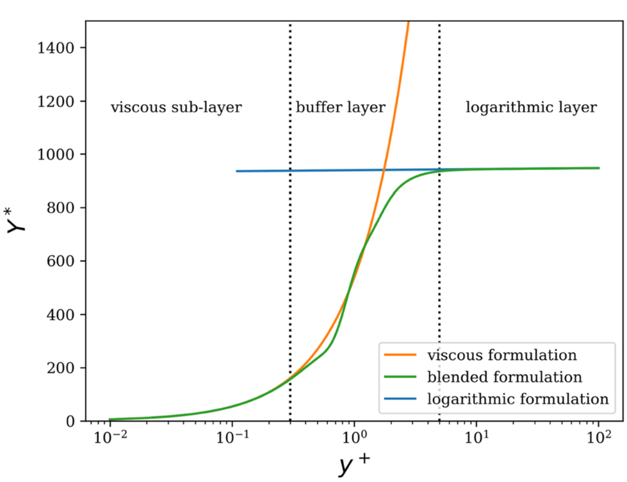

Fig. 3—Law of the wall for the dimensionless concentration based on the y^+-values. Due to the low diffusion coefficient, the boundary layer is very thin and can only be resolved with a fine mesh.

$$Y^* \equiv e^{\Gamma}\mathrm{Sc}y^* + e^{1/\Gamma}\mathrm{Sc}_t\left[\frac{1}{\kappa}\ln(\mathrm{E}y^*) + P_\mathrm{c}\right] \qquad [5]$$

where $\mathrm{Sc} = \nu/D_{ij}$ and $\mathrm{Sc_t} = 0.7$ are the molecular and turbulent Schmidt-numbers, $y^* \equiv \frac{\rho c_\mu^{\frac{1}{4}} k_p^{\frac{1}{2}} y_p}{\rho}$ is the dimensionless wall distance in analogy to y^+, κ is the von Karman constant, E is an empirical constant, and P_c is defined as:

$$P_\mathrm{c} = 9.24\left[\left(\frac{\mathrm{Sc}}{\mathrm{Sc_t}}\right)^{3/4} - 1\right]\left[1 + 0.28\mathrm{e}^{-0.007\mathrm{Sc}/\mathrm{Sc_t}}\right]. \qquad [6]$$

The blending function Γ is defined as:

$$\Gamma = -\frac{a(\mathrm{Sc}y^*)^4}{1 + b\mathrm{Sc}^3 y^*}, \qquad [7]$$

with $a = 0.01$ and $b = 5$, assuming the influence of heat-transfer and pressure gradients toward the wall to be negligible.

The diffusion flux $J_{i,w}$ of species i toward the wall equals the surface reaction rate. A quadratic growth law for the Fe_2Al_5 particles was presented in Reference 16:

$$J_{i,w} = K\rho_{\mathrm{Fe_2Al_5}}\frac{\gamma_i}{\gamma_{Fe_2Al_5}}\left(y_{i,w} - y_{i,w}^{eq}\right)^2, \qquad [8]$$

where K is the reaction kinetics constant, ρ is the density of the Fe_2Al_5 particles, γ_i is the stoichiometric coefficient and $y_{i,w}^{eq}$ is the equilibrium mass fraction at the wall based on thermodynamics.

Coupling Eq. [8] with Eq. [4] and using the blended Y^* value from Eq. [5], an iterative solution of the diffusion flux toward the wall and the wall concentration can be reached as shown in Figure 4.

C. *Design of Experiments*

A Design of Experiments (DoE) is set-up with the parameters listed in Table I. The Al concentration, the bath temperature, and the strip velocity were chosen to be varied in process relevant margins and set as boundary condition at the top of the domain (see

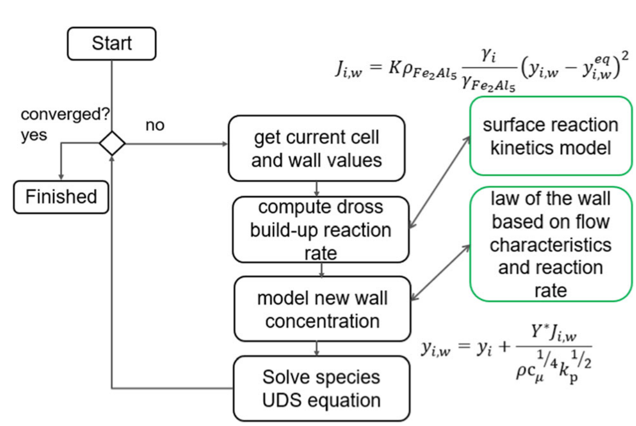

Fig. 4—Modeling workflow for the iterative computation of the wall concentrations and the wall reactions.

Table I. Summary of the DoE Parameters Used for the Simulation

DoE Parameters		
	min	max
Al (Wt Pct)	0.15	0.25
Bath Temperature (°C)	450	470
Strip velocity (m s^{-1})	2	3
Derived Parameters		
Fe (Wt Pct)	$Fe_{eq} * 1.1$	
Strip Entry Temperature (°C)	bath T + 5 °C	

Figure 2). A Latin Hyper-cube sampling[24] is applied to achieve an evenly distribution over the parameter space with 16 simulations. In addition to the DoE parameters in Table I that represent the process parameters, two derived parameters are fixed. The first parameter is the Fe concentration that is assumed to be slightly over-saturated by 10 pct and the second parameter is the strip entry temperature that is 5 °C above the bath temperature. The response value for the further data analysis is the averaged dross build-up rate on the bottom roll including the grooves.

D. *Data Analysis-Building of Process Model*

1. *Response Surface Method (RSM)*

The quadratic model to fit the optimal operating process parameters is:

$$Z = \alpha_0 + \sum_{i=1}^{k} \alpha_i X_i + \sum_{i=1}^{k} \alpha_{ii} X_i^2 + \sum_{i_{\leq j}}^{k} \sum_{j}^{k} \alpha_{ij} X_i X_j + \cdots + e \qquad [9]$$

where Z is the predicted response, X_i,X_j, ..., X_k are the input variables, X_i^2,X_j^2,..., X_k^2 are the square effects, X_iX_j,X_iX_k, and X_jX_k are the interaction effects, and α_i are the linear regression parameters and e is the model error. The statistical software *R Statistical Software (version 4.1.3 - 2022-03-10)*[25] was applied to test different models and to find the set of coefficients with the smallest error and the highest significance using the Analysis of Variance (ANOVA) method.[26]

2. *Neural Network (NN)*

In addition to classical RSM approaches, the DoE data were analyzed by the neural network package of *R*.[27] It applies the resilient backpropagation algorithm with weight backtracking, uses the logistic function as activation function and calculates the error based on the sum of squared errors.[28] To train the NN, 80 pct of the simulation data was randomly chosen and used as training data. Although it is known that neural networks, compared to RSM, require a significant larger amount of training data to build a reasonable model, it is tried with the available data and the performance of the two models are compared. The quality of the two approaches is obtained by the comparison of the coefficient of determination R^2:

$$R^2 = 1 - \frac{\sum_i (z_i - f_i)^2}{\sum_i (z_i - \bar{z})^2}, \qquad [10]$$

where $\bar{z}$ is the mean of the observed values z_i and f_i are the predicted values.

III. RESULTS AND DISCUSSION

In this chapter first the results of the CFD multi-physics model are described. Then the developed surrogate process model is discussed.

A. *Flow and Melt Conditions*

The flow conditions in the V-shape region are predominated by the steel-strip velocity. The pressure field together with the velocity vectors and the close-ups of the velocity distribution within the closed and open groove are shown in Figure 5 for a 1.5 mm thick strip with a velocity of 3 m s^{-1}, a bath temperature of 450 °C and an Al bath concentration of 0.164 wt pct. The additional boundary conditions are calculated according to Table I. At the first contact point between the steel strip and the sink roll, a higher pressure at this stagnation point can be observed, while at the other side, where the steel strip leaves the roll, a lower pressure is prevailing [see Figure 5(a)]. This pressure difference leads to an acceleration of the liquid Zn within the closed groove, so that the flow velocity of the liquid Zn exceeds the strip velocity [see Figure 5(c)]. This also leads to a lower pressure in the closed groove, which acts as an additional force on the steel strip. Another important aspect is the difference of the velocity profile in the closed and open groove as shown in Figures 5 (b) and (c). The closed groove shows a radial velocity profile with lower gradient, compared to the open groove, where a high velocity gradient can be observed. There, the velocity reduces by 50 pct in the first mm.

When comparing the concentration distributions of Fe and Al in the open and closed groove at the x = 0 position (rotation axis of the sink roll), a rather homogeneous distribution can be observed, with only slight differences in the concentrations (see Figures 6 (a) through (d) and Table II). These occur mainly for the Fe concentration at the strip interface, where a slight Fe dissolution from the steel strip through the inhibition layer is modeled[14].

To evaluate the effect of the steel-strip velocity and the immersing temperature on the actual dross build-up rate, additional simulations with the same bath temperature and Al concentration but slower strip velocity and a lower strip immersing temperature (+0 °C) were computed. The boundary conditions of the steel strip together with the averaged values in the closed and open groove are reported in Table II. A detailed evaluation of the local dross build-up rates at the $x = 0$ position (rotation axis of sink roll) are depicted in Figure 7.

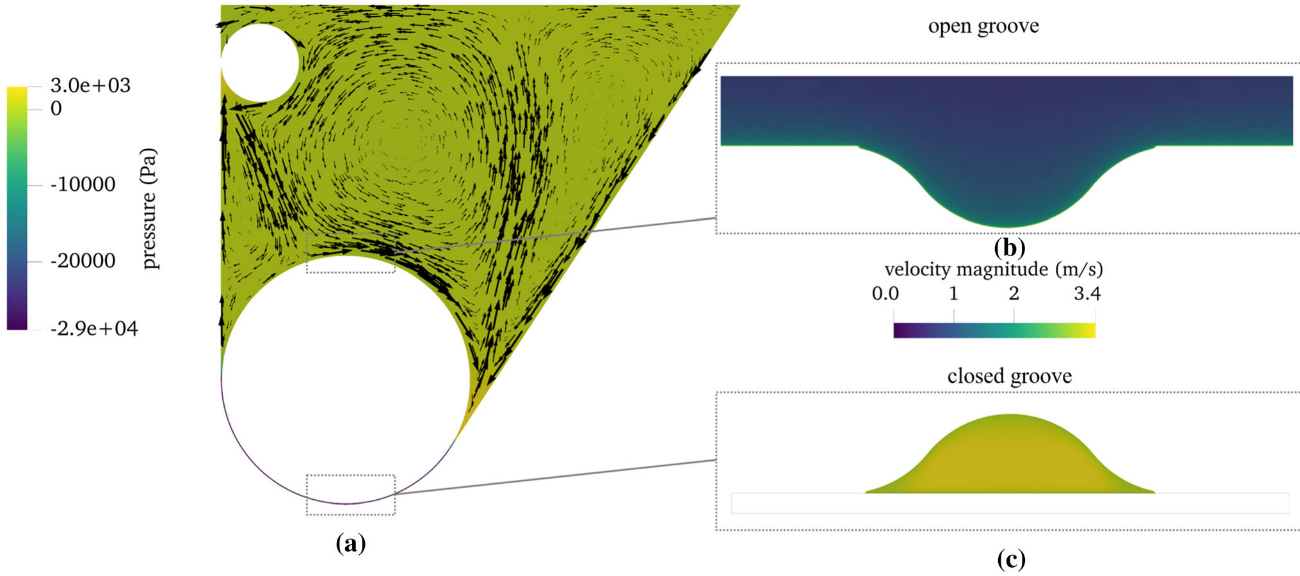

Fig. 5—Pressure distribution and velocity field in the V-shape region (*a*) and on the right side two slices at the $x = 0$ position corresponding to the rotation axis of the sink roll. (*b*) the open groove on top of the roll and (*c*) the groove covered by the strip (closed groove) at the bottom of the roll.

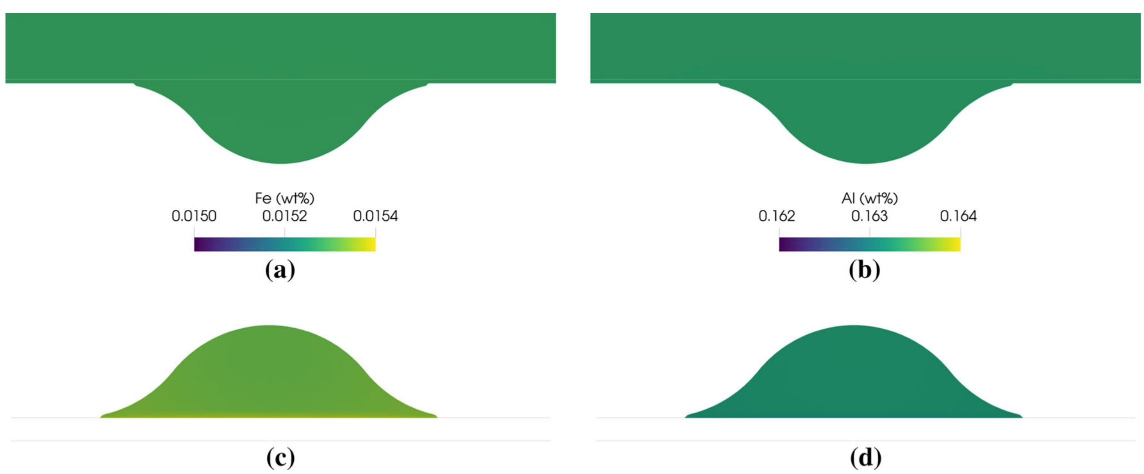

Fig. 6—Fe concentration in the open (*a*) and closed (*c*) groove, together with Al concentration in the open (*b*) and closed (*d*) groove at the x = 0 position. A very homogeneous concentration distribution can be observed.

Three important findings can be summarized: The first finding shows a significant effect of the strip immersing temperature on the overall dross build-up rate. In case of a colder immersing steel strip, the averaged dross build-up rate is higher by a factor of 2–3. In addition to that, a lower strip velocity leads to a further increase of the dross build-up rate in the case of a lower strip immersing temperature (+0 °C), when comparing [Figures 7(a) and (c)]. Having said that, in the case of a warmer immersing steel strip, this effect is reversed [(see Figures 7(b) and (d)]. Here, the faster moving steel strip brings in more energy and increases the temperature around the sink roll (see also Table II). This leads to a warmer micro climate and slightly shifts the equilibrium toward lower dross build-up rates.

The second finding focuses on the conditions in the grooves. For a warmer immersing steel strip (+5 °C), the dross build-up rate is slightly higher in the open groove [(see Figures 7(b) and (d)], while it is in the same range for the case of (+0 °C). This can be explained by the influence of the flow conditions on the mass transport toward the surface. In the case of (+0 °C)

Table II. Average Conditions of the Liquid Zn in the Closed and Open Groove for Different Strip Velocities and Strip Immersing Temperatures. A Slightly Warmer Immersing Steel Strip Leads to a Warmer Micro Climate Around the Role and thus to a Lower Dross Build-Up Rate

BC Immersing Strip	Groove	Al (wt pct)	Fe (wt pct)	T (°C)	Dross Build-Up Rate (kg m^{-2} s^{-1})
$v = 2$ m s^{-1} $T_{strip} = +\ 0$ °C	closed	0.163	0.0151	450.4	1.67e−6
	open	0.163	0.0151	450.4	1.62e−6
$v = 2$ m s^{-1} $T_{strip} = +\ 5$ °C	closed	0.163	0.0154	452.1	3.7e−7
	open	0.163	0.0153	451.9	5.4e−7
$v = 3$ m s^{-1} $T_{strip} = +\ 0$ °C	closed	0.163	0.0151	450.4	1.94e−6
	open	0.163	0.0151	450.4	1.91e−6
$v = 3$ m s^{-1} $T_{strip} = +\ 5$ °C	closed	0.163	0.0153	452.4	2.8e−7
	open	0.163	0.0153	452.2	4.3e−7

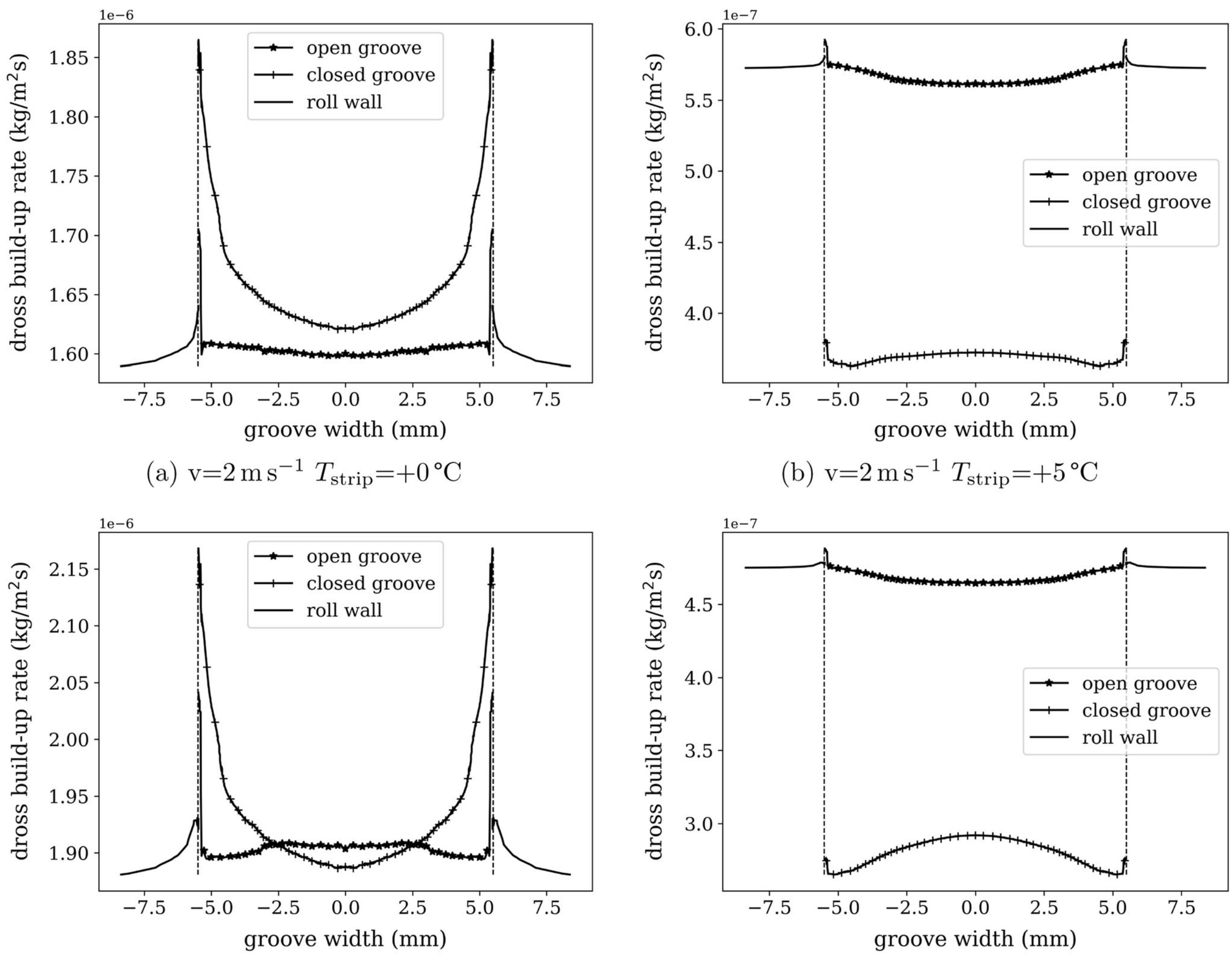

(a) v=2 m s^{-1} T_{strip}=+0 °C

(b) v=2 m s^{-1} T_{strip}=+5 °C

(c) v=3 m s^{-1} T_{strip}=+0 °C

(d) v=3 m s^{-1} T_{strip}=+5 °C

Fig. 7—Dross build-up rates at the x = 0 position in the closed and open groove. In general the dross build-up rates for the cooler immersing steel strip (+0 °C) are higher by a factor of 2-3. In addition to that, the dross build-up rates in the closed groove tend to increase toward the edges. Attention the scaling differs by a factor of 10 between $T_{strip} =\ +0$ °C and $T_{strip} =\ +5$ °C.

the thermodynamic conditions in the grooves are the same (see Table II) and a difference in the dross build-up rate depends mainly on the local flow conditions. In the case of (+ 5 °C), a warmer microclimate in the closed groove leads to a lower dross build-up rate although the Fe concentration is higher.

The third important finding is the fact that the dross build-up rate increases toward the edges of the groove. In terms of steel-strip surface quality this finding suggests that the time till the first crystals that grow in the grooves touch the steel strip is shorter, due to the higher growth rate and the smaller distance at the groove edges.

B. *Process Model*

The conducted DoE simulations with the influencing factors of Al concentration, bath temperature and strip speed (see Table I) were evaluated in terms of an averaged dross build-up rate on the roll and the grooves. The data were then used to build a process model with neural networks and linear regression modeling. The result of the neural network is plotted in Figure 8 with an R^2-value of 0.97. It turned out that using one hidden layer with three neurons is sufficient to yield a good agreement.

In the linear regression modeling, various models with increasing complexity were applied. The results are reported in Table III. All applied models are highly significant (*F* Statistic). It can be seen that the Al concentration, the bath temperature, and the interaction of the Al concentration and the temperature have the most significant effects according to their low *p*-values. In the linear regression modeling, the addition of the strip speed and the interaction between the strip speed and the temperature have a lower significance. Including higher-order terms in the model doesn't yield a better result. The highest R^2-value that can be achieved is 0.99 and thus slightly better than the neural network result. The advantage of the linear regression modeling is that a process model equation for the dross build-up rate R_d (kg $m^{-}2$ s^{-1}) can be determined:

$$R_d = -8.678\times10^{-5} + 3.267\times10^{-4}\mathrm{Al} + 1.935\times10^{-7}T + 6.018\times10^{-6}v - 1.315\times10^{-8}v*T - 7.289\times10^{-7}\mathrm{Al}*T, \qquad [11]$$

where *Al* is the concentration in (wt pct), *T* is the bath temperature in (°C), and *v* is the strip speed in (m s^{-1}). This model can be applied within the parameters given in Table I.

A comparison between the process model determined with the neural network and the linear regression modeling is depicted in Figure 9. It shows the very good agreement of the linear regression model and also between the trained NN-model and the test data.

The relative importance of the individual terms for the explanation of the R^2-value was calculated by the *R*-packages *relaimpo* based on normalized values.[29,30] The implemented method of Lindeman, Merenda, and Gold (lmg) was applied as its approach is appropriate to determine the causal importance of the regression parameters. The basic idea behind the metrics of lmg is based on the computation of sequential R^2s, but to take care of the dependence on orderings of the regression parameters by unweighted averaging over these orderings.[29] Figure 10 shows that the contribution of the Al concentration in the bath explain more than 60 pct of the R^2-value, and that the temperature and the interaction between the Al concentration and the temperature explain additional 35 pct, while the relative importance of the strip speed is below 5 pct.

The evaluation of the process model in Eq. [11] is summarized in Figure 11. It shows the contour plot of the dross build-up rate dependent on the temperature and Al concentrations at three fixed strip speeds (first

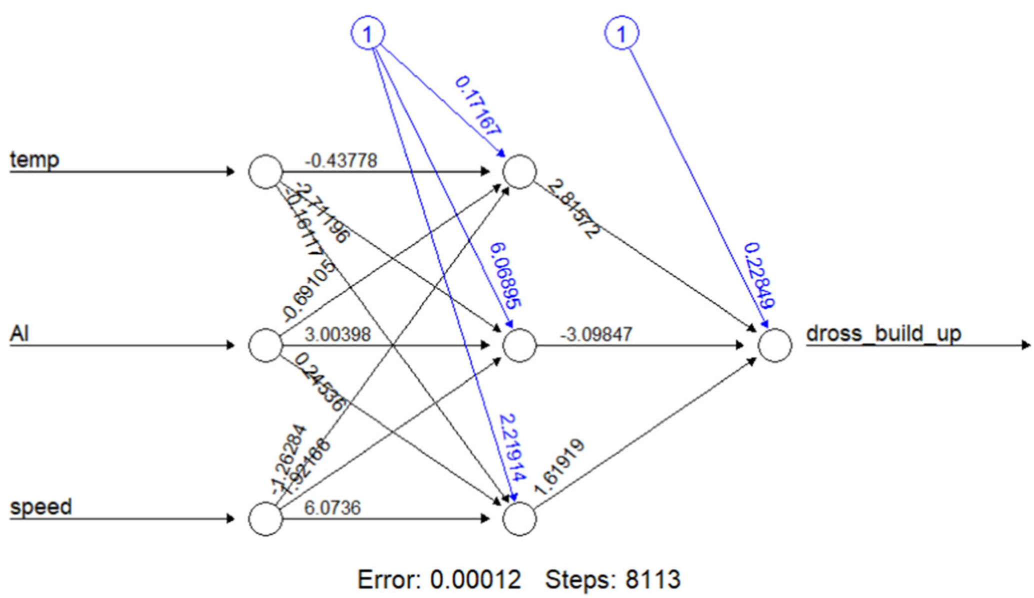

Fig. 8—Neural network including weights of the trained model. The first layer represents the input layer, the middle layer is the hidden layer with three neurons and the last layer is the output layer. The input parameters are multiplied by the computed weights and the blue lines represent an additional intercept value that is added to the weights (Color figure online).

Table III. Summary of the Linear Regession Model Parameters With Increasing Complexity

	Dependent Variable		
	Dross Build-Up		
	(1)	(2)	(3)
Al	− 8.476e−06***	3.037e−04***	3.267e−04***
	(1.138e−06)	(3.638e−05)	(3.571e−05)
Temp	2.409e−08***	1.515e−07***	1.935e−07***
	(5.840e−09)	(1.500e−08)	(2.548e−08)
Speed	− 3.896e−09		6.018e−06*
	(1.091e−07)		(3.065e−06)
Temp:speed			− 1.315e−08*
			(6.687e−09)
Al:temp		− 6.789e−07***	− 7.289e−07***
		(7.912e−08)	(7.763e−08)
Constant	− 8.940e−06***	−6.753e−05***	− 8.678e−05***
	(2.755e−06)	(6.901e−06)	(1.170e−05)
Observations	16	16	16
R^2	0.87	0.982	0.987
Adjusted R^2	0.838	0.977	0.98
Residual Std. Error	1.372e−07	5.137e−08	4.766e−08
F Statistic	26.809***	215.852***	151.236***
	(df = 3; 12)	(df = 3; 12)	(df = 5; 10)

*$p < 0.1$, **$p < 0.05$, ***$p < 0.01$.

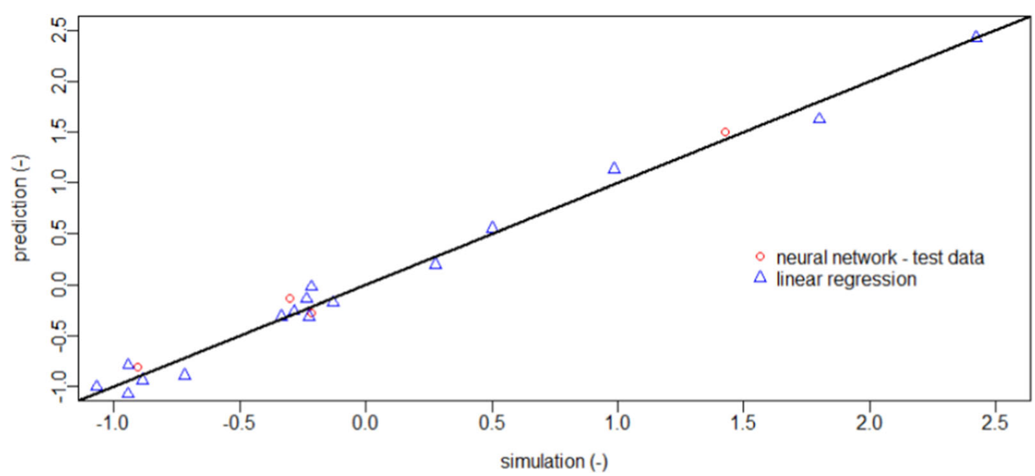

Fig. 9—Comparison between the simulated and the predicted normalized values of the neural network and linear regression process model. Both approaches are in good agreement.

row), dependent on the strip speed and Al concentration at three fixed temperatures (second row) and dependent on the strip speed and the temperature at three fixed Al concentrations (third row). In general, it can be observed that the dross build-up rate decreases with increasing Al concentration. That might be attributed to the fact that at higher Al concentration, the Fe dissolution from the steel strip is also lower and thus the main source of Fe in the zinc bath decreases. A second interesting aspect is that the dross build-up rate increases with increasing melt temperature at lower Al concentrations, while it is nearly independent of the temperature at higher Al concentrations.

When applying the process model to the actual zinc bath, the following limitations have to be considered: Firstly, the process model depends strongly on the applied boundary conditions for the underlying virtual DoE, especially on the presumed Fe supersaturation. In reality, the Fe supersaturation might depend more strongly on the strip speed, due to the fact that it also determines the amount of dissolved Fe in the bath. Secondly, the results are steady-state simulations, while in reality, the bath temperature and concentration will vary over time. This changes will shift the equilibrium of the system and thus the amount of Fe supersaturation.

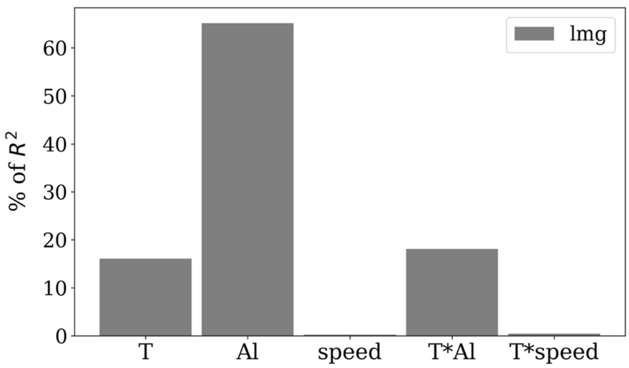

Fig. 10—Comparison of the relative importance of the individual terms in explaining their contribution to R^2 computed with the lmg method.[29,30] It can be seen that the Al concentration in the bath (> 60 pct), the temperature, and the interaction between Al and temperature has the highest importance (each $\sim$ 15 pct), while the influence of the speed is below 5 pct.

IV. CONCLUSION

A high fidelity model of the zinc bath was presented with the capability of coupling the surface reaction model for dross build-up with the mass transport via the wall function approach. This model was applied in a virtual Design of Experiment to determine the local dross build-up conditions on the sink roll surface. It was found that an increased dross build-up at the edges of the grooves is prevailing which might lead to surface coating defects. In addition to that, a process model was developed with the application of neural networks and classical linear regression modeling. The influence of the Al concentration has the highest influence on the dross build-up rate. In general, it was found that higher Al concentrations lead to lower dross build-up rates predicted by the model.

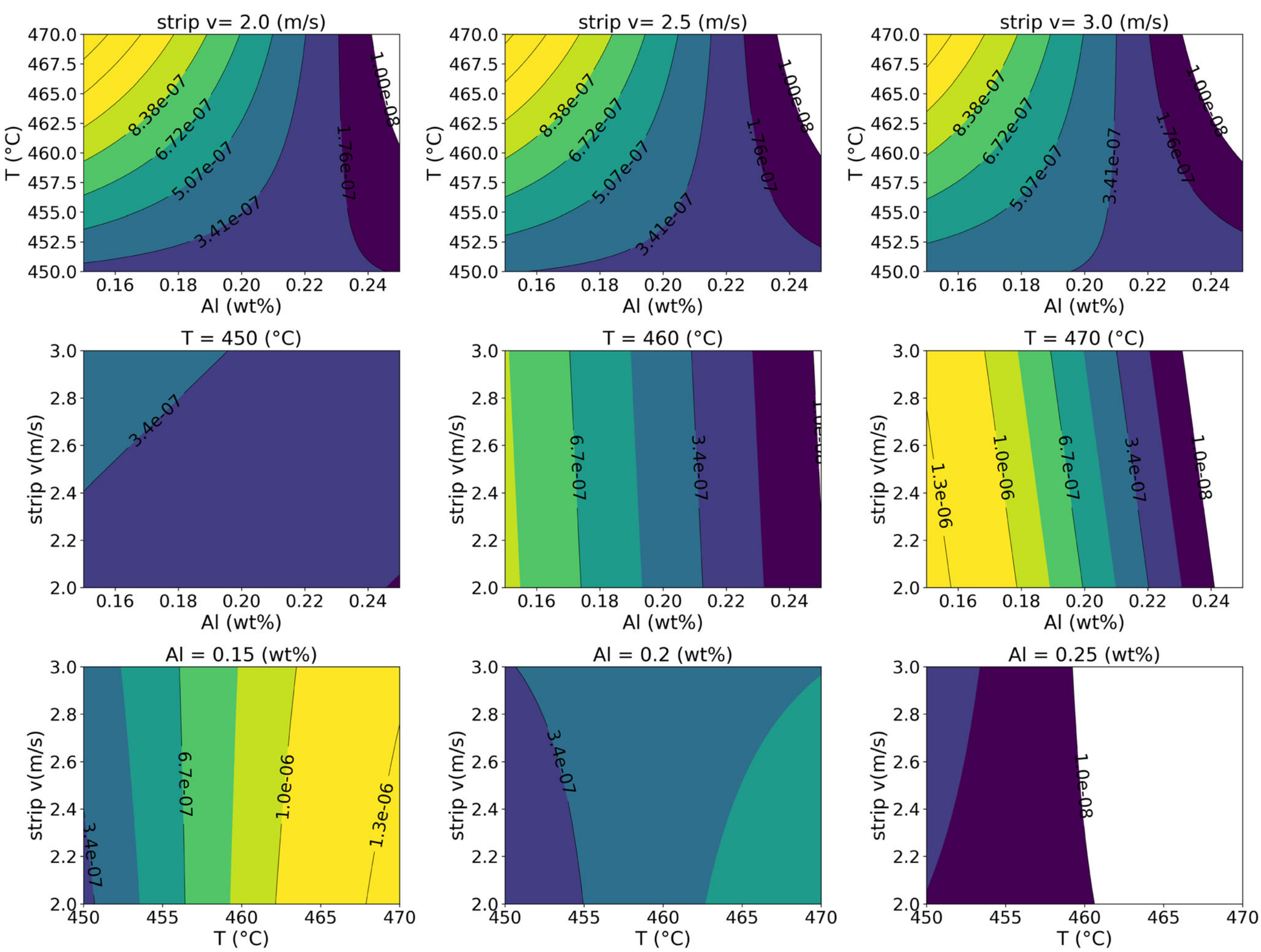

Fig. 11—Contour plot of the dross buil-up rate dependent on the temperature and Al concentrations at three fixed strip velocities (first row), dependent on the strip velocity and Al concentration at three fixed temperatures (second row), and dependent on the strip velocity and the temperature at three fixed Al concentrations (third row).

ACKNOWLEDGMENTS

The authors gratefully acknowledge the financial support under the scope of the COMET program within the K2 Center "Integrated Computational Material, Process, and Product Engineering (IC-MPPE)" (Project No 886385). This program is supported by the Austrian Federal Ministries for Climate Action, Environment, Energy, Mobility, Innovation and Technology (BMK) and for Labour and Economy (BMAW), represented by the Austrian Research Promotion Agency (FFG), and the federal states of Styria, Upper Austria, and Tyrol. Furthermore, the authors would like to thank Daniel Scheiber for his feedback on the neural network and Michel Dubois for providing the figure of the dross build-up on the bath roll.

CONFLICT OF INTEREST

The authors declare that they have no conflict of interest.

REFERENCES

1. R. Thiounn, M. Simonnet, L. Pineau, C. Dulcy, Y. Hardy, J. Hagler, G. Wiedner, and P. Foerster: *Iron Steel Technol.*, 2004, vol. 1, pp. 31–37.
2. A. Nag, M.K. Bhadu, P.K. Bijalwan, and A.S. Pathak: *Corrosion Sci.*, vol. 180, p. 109177 (2021). https://doi.org/10.1016/J.CORSCI.2020.109177.
3. B.G. Seong, S.Y. Hwang, M.C. Kim, and K.Y. Kim: *Surf. Coat. Technol.*, 2001, vol.138, p. 101. https://doi.org/10.1016/S0257-8972(00)01136-1.
4. H. Wang, F. Tang, J. Chen, M. Xing, X. Liu, X. Song *Corrosion Sci.*, 2022, vol. 199, p. 110192 https://doi.org/10.1016/J.CORSCI.2022.110192.
5. H. Nitta and A. Tsuyuki: Pot roll for continuous hot-dip galvanizing. 1995.
6. L. Kümmel, J. Bergern, W. Unterberg, N. Brendel, and T. Stoltenhoff: Component for a hot dip coating system and method for the production thereof. 2017. https://patents.google.com/patent/WO2017186461A1/en.
7. J. Nakano, G.R. Purdy, and D. Malakhov: in GalvaTech, 2007, pp. 135–140.
8. J. Nakano: A computational thermodynamic study of the systems Zn–Fe and Zn–Fe–Al. Ph.D. thesis, McMaster University. 2006.
9. F. Ilinca, F. Ajersch, C. Baril, and F.E. Goodwin: *Int. J. Numer. Meth. Fluids*, 2007, 53(10), p. 1629.
10. F. Ajersch, F. Ilinca and F.E. Goodwin: in Materials Science and Technology Conference and Exhibition. 2013, vol. 2, pp. 1145–52.
11. X. Zhou, S. Yuan, Y. Huang, P. Yang, and X. Zhou: *Ironmak. Steelmak.*, 2015, 42(10), p. 785.
12. K.R. Yu, F. Ilinca, and F.E. Goodwin: in AISTech-Iron and Steel Technology Conference Proceedings, 2016, vol. 2, pp. 2043–53.
13. F. Ajersch and F. Ilinca: *Steel Res. Int.*, 2018, vol. 89, p. 1700074.
14. G. Reiss, A. Ishmurzin, C. Mugrauer, W. Eßl, W. Ecker, J. Strutzenberger, H. Unger, and G. Angeli, *Metall. Mater. Trans. B*, 2019, vol. 50(2), p. 834.
15. G. Reiss, W. Eßl, J. Strutzenberger, R.A. Trasca, H. Unger, and G. Angeli: *Metall. Mater. Trans. B*, 2022, vol. 53, p. 3833. https://doi.org/10.1007/S11663-022-02645-9.
16. M. Stefan-Kharicha, A. Kharicha, K. Zaidat, G. Reiss, W. Eßl, F. Goodwin, M. Wu, A. Ludwig, and C. Mugrauer: *J. Crystal Growth*, 2020, vol. 541, p. 125667.
17. D. Scheiber, W. Eßl, J. Strutzenberger, F. Goodwin, J. Spitaler, and G. Reiss: *J. Alloys Compds.*, 2020, vol. 824, p. 153854.
18. H.K. Versteeg and W. Malalasekera: *An Introduction to Computational Fluid Dynamics. Longman Scientific & Technical*, 1995.
19. J.H. Ferziger and M. Peric: *Computational Methods for Fluid Dynamics*. Springer, Berlin, 2002.
20. R. Schwarze: *CFD-Modellierung. Grundlagen und Anwendungen bei Strömungsprozessen* Springer, 2013.
21. D. Scheiber, W. Eßl, J. Spitaler, and G. Reiss: *Acta Materialia*. 2023, p. 119423. https://doi.org/10.1016/j.actamat.2023.119423.
22. J. Bredberg:. On the wall boundary condition for turbulence models, 2000. https://www.researchgate.net/publication/255608559_On_the_Wall_Boundary_Condition_for_Turbulence_Models. Accessed: 28 Aug 2022.
23. B.A. Kader: *Int. J. Heat Mass Transf.*,1981, vol. 24, p. 1541.
24. M.D. McKay, R.J. Beckman, and W.J. Conover, *Technometrics*, vol. 21, p. 239. https://doi.org/10.2307/1268522.
25. R Core Team: *R: A Language and Environment for Statistical Computing. R Foundation for Statistical Computing*, Vienna, 2022. https://www.R-project.org/.
26. J.M. Chambers and T. Hastie: *Statistical models in S*, 1st edn. Chapman and Hall/CRC, (1992). https://www.routledge.com/Statistical-Models-in-S/Chambers-Hastie/p/book/9780412830402.
27. S. Fritsch, F. Guenther, and M.N. Wright: Neuralnet: Training of Neural Networks, 2019. https://CRAN.R-project.org/package=neuralnet. R package version 1.44.2.
28. M.A. Riedmiller: Rprop-description and implementation details, 1994.
29. U. Grömping: *J. Stat. Softw*. 2006, vol. 17(1), p. 1.
30. U. Grömping: *Comput. Stat.*, 2015, vol. 7, p. 137 https://doi.org/10.1002/WICS.1346.